J. Fluid Mech. (1995), vol. 302, pp. 149–178

The effect of vortex pairing on particle dispersion and kinetic energy transfer in a two-phase turbulent shear layer

By KENNETH T. KIGER AND JUAN C. LASHERAS

Department of Applied Mechanics and Engineering Sciences,
University of California at San Diego, La Jolla, CA 92093-0411, USA

(Received 21 June 1994 and in revised form 20 April 1995)

The transport of heavy, polydispersed particles and the inter-phase transfer of kinetic energy due to the viscous drag forces is measured experimentally in a turbulent shear layer. To study the effect of the large-scale vortex pairing event, the shear layer is forced simultaneously with a fundamental and subharmonic perturbation. It is shown that vortex pairing plays a homogenizing role on the particulate field, but the amount of homogenization is strongly dependent upon the particle's viscous relaxation time, the eddy turnover time, as well as the time the particles interact with each scale prior to a pairing event. Thus, even though the smaller size particles become well-mixed across the large eddies, the larger sizes are still dispersed in an inhomogeneous fashion. It is also found that the kinetic energy transfer between the phases occurs inhomogeneously with energy being exchanged predominantly in a sublayer just outside the region of maximum turbulence intensity. The kinetic energy transfer is shown to exhibit notable positive and negative peaks located beneath the cores and stagnation points of the large-scale eddy field, and these peaks are shown to result from the irrotational velocity perturbations created by the vortices. This energy exchange mechanism remains a prominent process as long as the Stokes number of the particles relative to the vortices is of order unity.

1. Introduction

Particle-laden turbulent flows are often encountered in a wide variety of natural and engineering applications. Of fundamental importance to these two-phase applications is the ability to predict not only how the particulate is dispersed by the turbulence, but also how the presence of the particulate may affect the evolution of the turbulent carrier fluid. The conservation equations governing the development of a two-phase, turbulent flow require a description of the inter-phase mass, momentum, and energy transport. Owing to a lack of information on the details of the complex processes involved, these terms are often postulated by *ad hoc* scaling arguments and intuitive reasoning. The two-phase, turbulent, planar mixing layer is one such example where inhomogeneities and anisotropies of the underlying flow make such closure assumptions of limited or no use. Thus, the experimental characterization of the dispersion and inter-phase kinetic energy transport in a prototypical, turbulent shear layer represents an important step towards the general formulation of two-phase flows.

Since the work of Winant & Browand (1973) and Brown & Roshko (1974), it

is well known that a turbulent shear layer exhibits the presence of large-scale, coherent, vortical structures superimposed on a small-scale three-dimensional motion. Furthermore, it is known that the kinematic interaction of these large-scale eddies (also known as vortex pairing) is responsible for the growth of the mixing region (Winant & Browand 1973).

Previous experimental (Lázaro & Lasheras 1992*a,b*) and numerical (Martin & Meiburg 1994; Crowe, Chung & Troutt 1988; Chein & Chung 1988) studies of the early evolution of a two-phase turbulent shear layer have shown that the large-scale coherent motion plays a dominant role in the particulate dispersion process. As the mixing layer grows through subsequent vortex pairings, the question which remains to be elucidated is how this event contributes to the inter-phase transport terms, and thus, to the particulate dispersion process. Towards this goal, we have conducted an experimental study of a turbulent, plane free shear layer in which the pairing event has been localized by forcing with a principal and the first subharmonic wave. In order to isolate the characterization of the kinetic energy from the mass and thermal energy transfer terms, we studied an isothermal (non-vaporizing) polydispersed water spray in a two-dimensional shear layer. Conditional sampling was used to provide a detailed examination of the dispersion and kinetic energy transfer between the phases due to the particle's drag both prior and during the vortex pairing event. Following this approach, we are able to provide not only a detailed characterization of the inter-phase kinetic energy transfer when the shear layer is dominated by the presence of one large coherent scale, but also to investigate the evolution of this energy transfer as a new scale, twice the original size, emerges through the pairing process.

2. Experimental facility and measurement techniques

The experimental facility utilized the output of a multi-phase, low-speed wind tunnel to form a free shear layer with the ambient, stagnant air (figure 1). The facility was the same one used in the studies of Lázaro & Lasheras (1989, 1992*a,b*), and was modified only in the course of routine operative maintenance. The test section itself was 26 cm wide, 45 cm deep, and 100 cm long. A two-dimensional instrument traverse allowed measurement access to the first 33 cm past the splitter plate in the streamwise (x) direction, and to 19 cm in the cross-stream (y) direction.

In order to increase the coherence of the naturally evolving large-scale vortices of the shear layer, a forcing system was used to add a velocity perturbation at the beginning of the test section. The system consisted of a speaker attached to a small plenum chamber ($25 \times 12 \times 2$ cm) which terminated at the end of the splitter plate with a narrow, spanwise slot. To obtain a consistent pairing within the confines of the measurement region ($\sim$ 33 cm), the flow was forced with both a fundamental and its first subharmonic frequency. The fundamental frequency was selected to be 140 Hz, which was close to the most unstable frequency of the unforced shear layer (Lázaro & Lasheras 1992*a*). After sampling the amplified signal sent to the speaker, the shape of the waveform was found to have the functional form

$$\sin(2\pi f_s t) + 1.93\sin(4\pi f_s t - \Delta\phi), \tag{2.1}$$

where f_s is the first subharmonic frequency (70 Hz), and $\Delta\phi$ is the phase difference between the fundamental and subharmonic, measured to be 212°. Yang & Karlsson (1991) have observed that for equal-amplitude waves, $\Delta\phi \sim 90^o$ results in a 'tearing' growth of the vortices, whereas all other phase angles resulted in a pairing event similar to one observed by Winant & Browand (1973). Thus, as can be confirmed

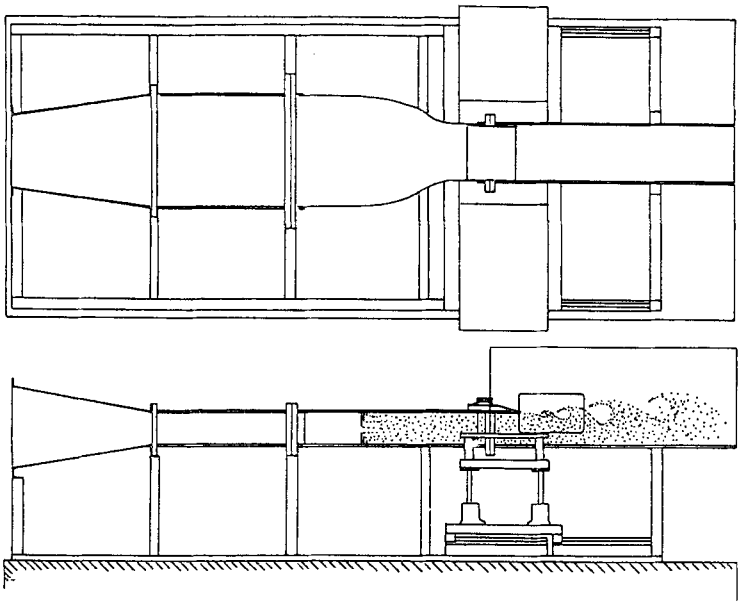

FIGURE 1. Schematic of wind tunnel facility

by the experimental data (see figure 3), a repeatable pairing event occurs in the test section of the facility.

Two different optical measurement techniques were used to quantify the evolution of the shear layer and the spray: instantaneous laser attenuation and phase Doppler anemometry. In developing the first technique, Lázaro & Lasheras (1992*a*) showed that the attenuation of a laser beam passed through a dilute spray of spherical particles can be described by

$$\xi \equiv -\ln\left(\frac{I}{I_o}\right) = 3\alpha L \int_0^\infty \frac{\mathrm{pdf}\,(D)}{D}\mathrm{d}D, \tag{2.2}$$

where I/I_o is the ratio of the attenuated/unattenuated laser beam intensity, L is the beam's path length through the spray, α is the average droplet volume concentration along the beam, D is the droplet diameter, and pdf(D) is the spanwise average volume probability density function of the spray. In this experiment, a 5 mW He-Ne laser was spatially filtered to produce a nominal 3.5 mm beam diameter. A LeCroy 8212A data logger was used to simultaneously digitize the laser attenuation and the speaker forcing signal using a sampling rate of 5000 Hz and record lengths of 32 768 points, producing time traces spanning the passage of more than 450 subharmonic structures.

Measurements were also made with an Aerometrics two-component Phase-Doppler Particle Analyzer (PDPA) (Bachalo & Houser 1983; Sankar & Bachalo 1991). This instrument operates on the same principle as a laser Doppler velocimeter (Drain 1980) with the added capability of measuring the size of the scattering droplet. This allows the PDPA to collect statistics on the size and two components of the velocity of droplets passing through the probe sampling volume. Except for a few locations in the external region of the mixing layer where the data rates became extremely slow owing to the sharp decrease in particle concentration, each data record was composed of 10 000 samples.

The initial conditions selected for this study are presented in figure 2. Figure 2(*a*)

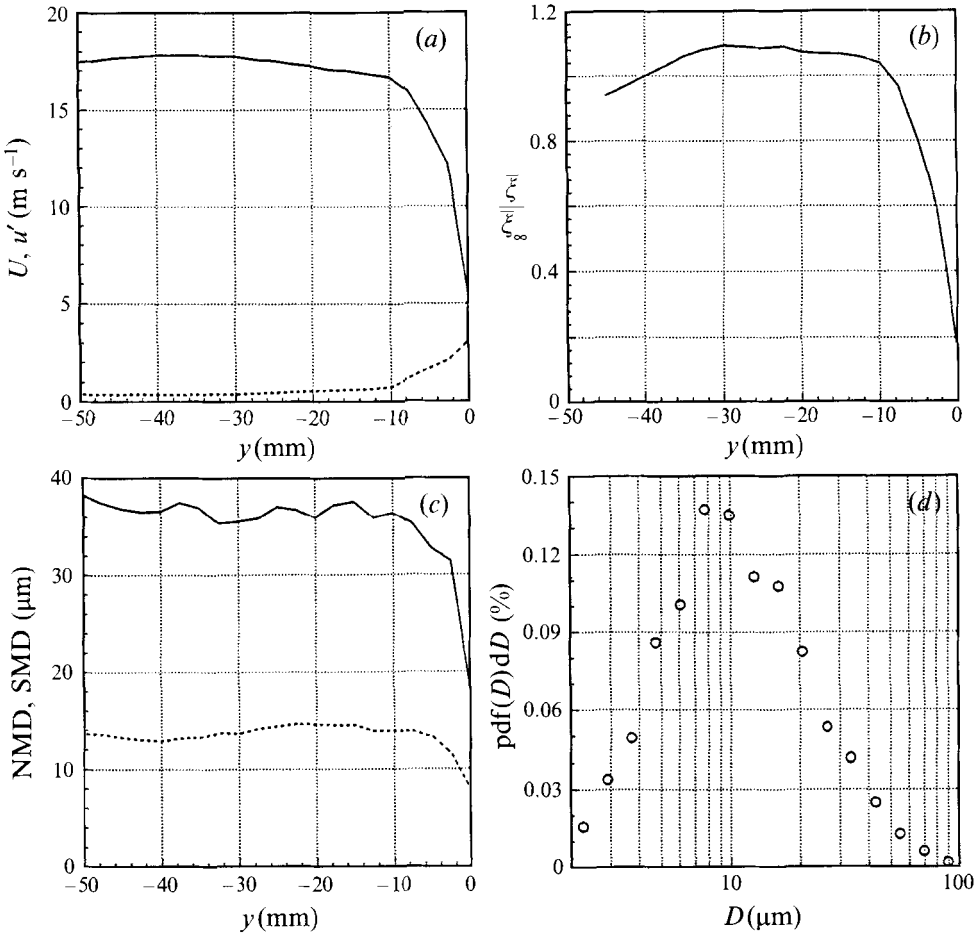

FIGURE 2. Initial conditions of facility. (*a*) Mean and r.m.s. streamwise gas velocity profile at $x = 0.7$ cm. ——, U; ----, u'. (*b*) Normalized laser attenuation profile at $x = 0$ cm. Profile normalized by average attenuation at $y = -4$ cm. (*c*) Cross-stream profiles of Sauter mean diameter (SMD, ——) and number mean diameter (NMD, ----) at $x = 0.7$ cm. (*d*) Number probability distribution function, pdf(D), of the spray at $x = 0.7$ cm, $y = -3$ cm.

shows the uniformity of the carrier gas velocity with a mean free-stream value of approximately 18 m s^{-1}, a 1 cm boundary layer level thickness, and an initial momentum thickness (θ_m) of approximately 1.5 mm. The r.m.s. velocity measurements show that the free-stream turbulence intensities are less than 2%, with the presence of a highly turbulent boundary layer (tripped by the rough absorbency material and the forcing fluctuations) having intensities on the order of 17%. Figure 2(*c*) shows that the Sauter mean diameter (SMD), D_{32}, and number mean diameter (NMD), D_{10}, as defined by

$$D_{mn} = \left[\frac{\int_0^\infty D^m \mathrm{pdf}(D)\,\mathrm{d}D}{\int_0^\infty D^n \mathrm{pdf}(D)\,\mathrm{d}D} \right]^{\frac{n+1}{m}}, \tag{2.3}$$

also have relatively uniform distributions of approximately 35 and 10 μm, respectively,

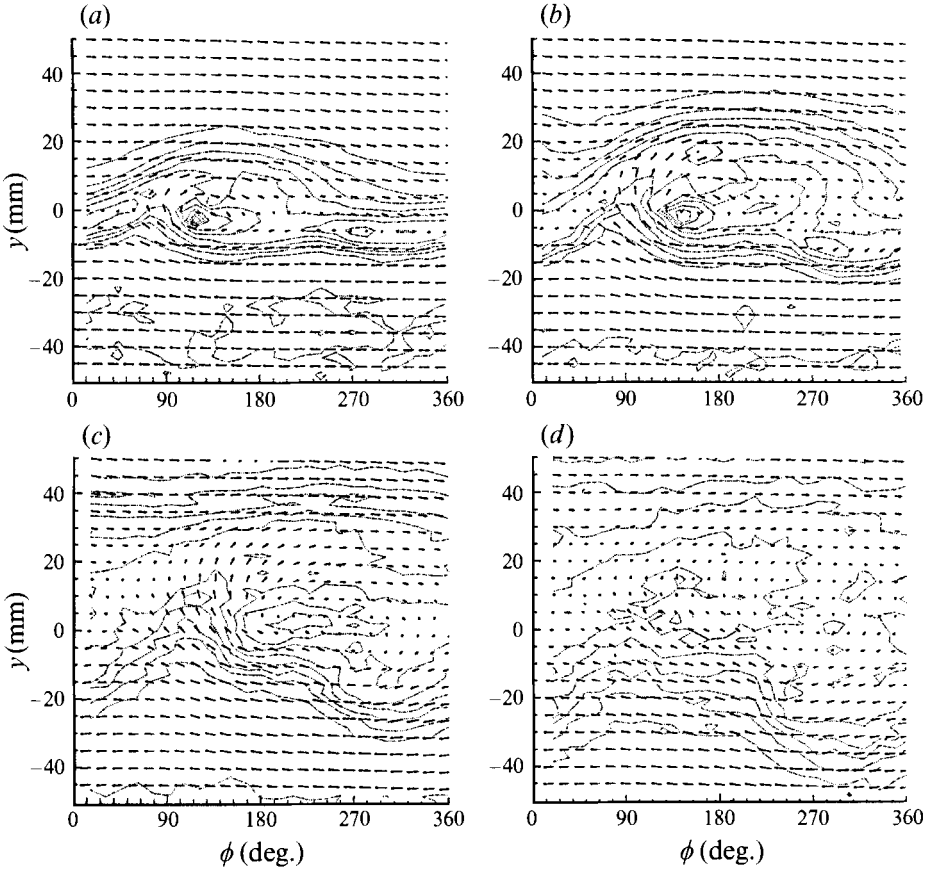

FIGURE 3. Conditionally averaged r.m.s. velocity contours and velocity vector plots for the carrier gas. Flow is from right to left for the lower stream ($y < 0$) and $\overline{U} = 9$ m s^{-1} has been subtracted from the streamwise component to show the vortex structure. (*a*) $x = 6$ cm, (*b*) $x = 10$ cm, (*c*) $x = 18$ cm, (*d*) $x = 30$ cm.

and a boundary layer level thickness of 1 cm. A representative size distribution (figure 2*d*) shows that it is quite polydispersed, spanning approximately two decades from 1 to 100 μm. Finally, the normalized mean attenuation measurements of figure 2*b* show the overall droplet concentration to be constant over the cross-stream coordinate, with a decay in the boundary layer (due to particle settling effects in the slower stream) and a slight drop-off in the deep free-stream for $y < -35$ mm. These measurements, in conjunction with the size distribution, gives a free-stream particle volume fraction of $\sim 1.5 \times 10^{-5}$.

The evolution of the carrier gas was extensively measured in the absence of the spray by seeding both the ambient air and the high-speed stream with fine water droplets and using the PDPA to measure their size and velocity at various regions in the flow. During the measurements, all of the air jets in the atomizer grid were kept on, but their water supply was cut off to prevent seeding bias problems between the two streams. Two-dimensional velocity bias corrections were made to the data utilizing a scheme similar to that proposed by McLaughlin & Tiederman (1973)†.

† At the time of the measurements, the PDPA did not provide particle residence times inside the probe volume which would have allowed for more accurate corrections.

The large-scale vortices and their pairing can be observed in greater detail through conditional-averaged velocity vector plots and the conditional-averaged r.m.s. velocity (figure 3). Initially, two vortices of slightly different strength (owing to the finite amplitudes of the principal and subharmonic forcing components) form at the fundamental wavelength. The vortices grow, initiate a pairing around $x = 12$ cm, and exit the measurement section ($x = 33$ cm) as a single subharmonic structure. The total r.m.s. is constructed from the sum of each velocity component's variance within a single phase-averaging bin. This represents the presence of small-scale random fluctuations and contributions due to temporal gradients in phase-averaged velocity between the beginning and ending times of the individual bin. As can be seen from figure 3, the r.m.s. effectively marks the cross-stream extent of the mixing layer and shows the location of the vortex cores and braid regions in the flow.

3. Results and discussion

3.1. *Particulate evolution: pre-pairing dispersion*

Information on the time evolution of the instantaneous particle dispersion process was obtained through measurements of the laser attenuation. The coherence of the particle concentration field in the large-scale vortices can be analysed by the attenuation Eulerian temporal correlation coefficient, which is written as

$$R_{\xi\xi}(\tau) = \frac{\lim\limits_{T\to\infty} \frac{1}{T}\int_0^T \xi(t)\xi(t+\tau)\mathrm{d}t}{\lim\limits_{T\to\infty} \frac{1}{T}\int_0^T \xi(t)\xi(t)\mathrm{d}t}, \tag{3.1}$$

where $\xi(t)$ is the measured attenuation. For our flow, $R_{\xi\xi}(\tau)$ is a periodic function composed of two frequencies (the fundamental and subharmonic) with a slightly decaying amplitude (figure 4). As seen by comparing the subharmonic peaks ($\tau = 14$ and 28 ms), the amplitude is never less than 0.84, indicating a very high degree of repeatability between structures. The evolution of the $R_{\xi\xi}(\tau)$ also connotes a change of dominant length scale within the test section. Initially, the fundamental frequency is dominant, but by the end of the test section only the subharmonic remains, demonstrating the occurrence of a pairing event. The location of the pairing within the test section can be more precisely defined by considering the development of the fundamental and subharmonic peaks of the attenuation spectra (Huang & Ho 1982) (figure 5). The spectral peaks show that the fundamental is dominant throughout the first 12 cm of the shear layer, growing, saturating, and then beginning to decay. At the end of this region, the subharmonic becomes dominant, marking the initiation of the pairing. This conveniently defines the regions of interest for our flow: (I) the region of the developing fundamental disturbance ($x = 0$ to 12 cm), (II) the transitional pairing event (the region where the subharmonic and fundamental scales have comparable amplitude) ($x = 12$ to 20 cm) , and (III) the resulting subharmonic structure ($x = 20$ to 30 cm).

The large degree of structure repeatability demonstrated by the $R_{\xi\xi}(\tau)$ implies that it is feasible to obtain a clear picture of how the large-scale vortices disperse the droplets by performing an ensemble average over a large number of structures. Using the waveform sent to the forcing generator as a phase reference signal, one can construct a conditional-average of the instantaneous signal, giving a portrait of an average dispersion structure. The conditional average, denoted by $\langle\rangle$, is defined for

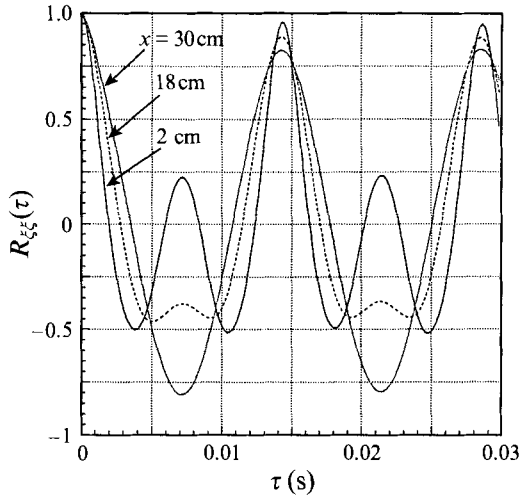

FIGURE 4. Attenuation Eulerian temporal correlation coefficient evolution along cross-stream location of peak r.m.s. fluctuations.

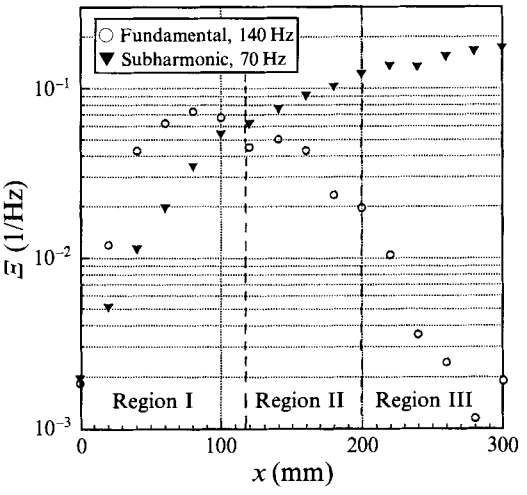

FIGURE 5. Evolution of attenuation spectral peaks corresponding to the fundamental and first subharmonic instability frequencies.

the attenuation as follows (Kiger 1995):

$$\langle \xi(\phi_i) \rangle = \frac{\lim_{T\to\infty} \frac{1}{T} \int_0^T \xi(t) I(\phi_i, t) \mathrm{d}t}{\lim_{T\to\infty} \frac{1}{T} \int_0^T I(\phi_i, t) \mathrm{d}t}, \tag{3.2}$$

where ϕ_i is the phase angle of the forcing function over one subharmonic period, t is the time of the recorded signal, and $I(\phi_i, t)$ is the conditioning function that selects what region of the data signal is used to produce the average. For our experiment, the conditioning function is a periodic square wave pulse that has a duration equal to the bin width of the averaging, $\Delta\phi$, and a frequency equal to the subharmonic

forcing component:

$$I(\phi_i, t) = \begin{cases} 1 & \text{for } (i - 1/P < t \bmod 1/f_s < i/P \\ 0 & \text{for all other } t \end{cases}, \quad i = 1 \text{ to } P, \tag{3.3}$$

where P is the number of bins in one wavelength ($P = 2\pi/\Delta\phi$).

One of the goals of this work is to quantify the role vortex pairing plays in the dispersion process, especially in contrast with the mechanisms found in the initial developing region. Lázaro & Lasheras (1992*b*) studied this case in detail and presented measurements sampled from a shear layer forced with only a single frequency. Owing to the similarity of the experimental facility, their work will be used as a direct comparison between the two cases. Dispersion characteristics found to be consistent with the regime studied by Lázaro & Lasheras (1992*b*) will henceforth be referred to as the single frequency forcing case, whereas the results from the current study will be denoted as the pairing mode forcing case.

In region I of the pairing mode forcing case (figure 6), we observe the same dispersion characteristics found in the single frequency forcing results: namely, particle dispersion across the mixing layer is manifested in the form of a well defined streak originating near the free stagnation point, and is entrained over the core of the vortex (cf. figure 6*b*, the pattern is clearly depicted within the larger vortex on the left-hand side; the asymmetry is due to the finite subharmonic component initially present). As the flow evolves, the streak grows, increasing in concentration and azimuthal extent as the droplets begin to respond to the coherent fluctuations. Thus, it is clearly evident that the entrainment process due to a single dominant frequency produces strong inhomogeneities across the vortex and leaves the core depleted of all but the smallest droplets. This initial interaction process leading to the non-uniform particle concentration can be understood in view of the magnitude of the forces acting on the particle (drag, buoyancy, etc.) as it interacts with a single vortex structure (Lasheras & Tio 1994).

In the transition region where both scales begin to interact, region II, the attenuation images provide an overview of the droplet dispersion during the pairing process (figures 6*c–e*). Here the pairing is initiated, and the smaller vortex on the upstream side is beginning to amalgamate with the larger, downstream vortex. As the pairing takes place, the droplets that had been entrained by the smaller streak are dispersed into the rapidly evolving core of the subharmonic structure. This results in a final structure (region III, figure 6*f*) that seems to be quite different from the original one – the streak is much broader and more diffuse while the core is no longer depleted of particles. Thus, it is noted that the pairing tends to have a homogenizing effect on the dispersion, reducing the particle concentration gradients within the vortex. It should be realized, however, that the particles are not passive scalars, and each droplet size responds to this process differently. These size-dependent effects are not readily apparent in the attenuation measurements, which are quantities integrated over all size classes in the flow. The size-dependent dispersion considerations will be expanded upon in the next section.

Further evidence of the contrasting mixing processes taking place in the two regions can be seen through the evolution of the r.m.s. attenuation profiles (figures 7 and 8). For single frequency forcing, the r.m.s. profiles were found to exhibit a peak in the lower central region of the mixing layer which increased throughout most of the test section (figure 8*a*). At $x = 200$ mm, however, the amplitude underwent a sudden decrease, and rapidly moved into the lower edge of the mixing region (figure 8*a,b*).

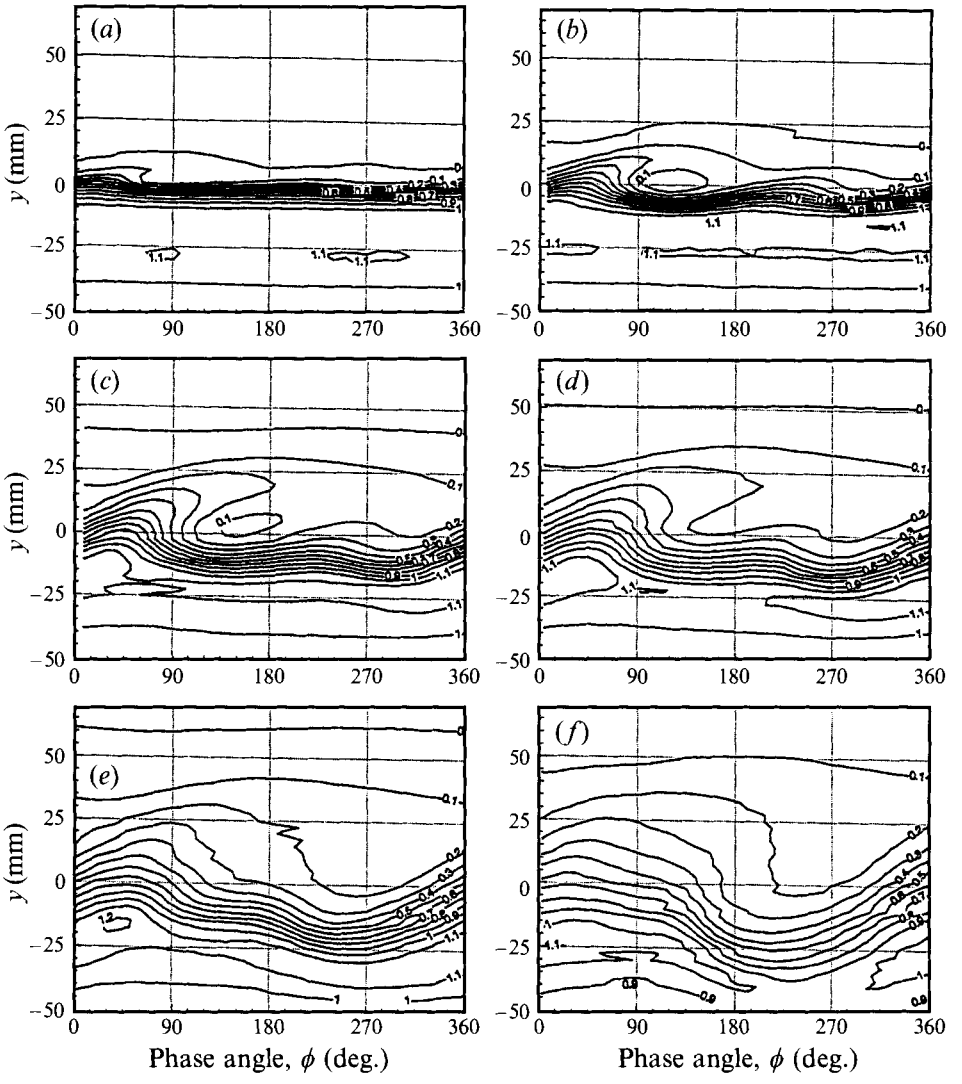

FIGURE 6. Contours of the conditional-averaged laser attenuation, ξ. Surfaces have been normalized by the averaged attenuation at $y = -4$ cm. Region I: (*a*) $x = 2$ cm, (*b*) $x = 6$ cm; Region II: (*c*) $x = 14$ cm, (*d*) $x = 18$ cm; Region III: (*e*) $x = 22$ cm, (*f*) $x = 30$ cm.

Lázaro & Lasheras attributed this behaviour to the presence of a well-developed, extended streak. Initially, the largest attenuation fluctuations occurred when the beam alternately passed through the low-attenuation region in the vortex core and the high-attenuation region in the base of the streak. As the streak evolved and the concentration increased along its length, the fluctuation levels increased with it. The peak decay and location shift occurred when the streak developed to such a point that it impacted on the upstream neighbouring vortex. The r.m.s. level was then reduced due to the lengthened duty cycle of the heightened attenuation and the maximum shifted to a location deeper in the spray. The existence of an external plateau was also attributed to an extensive streak development, as the r.m.s. was stabilized by the increased signal duty cycle and attenuation decayed along the streak.

Comparing the above results with the pairing mode forcing shows the similarities

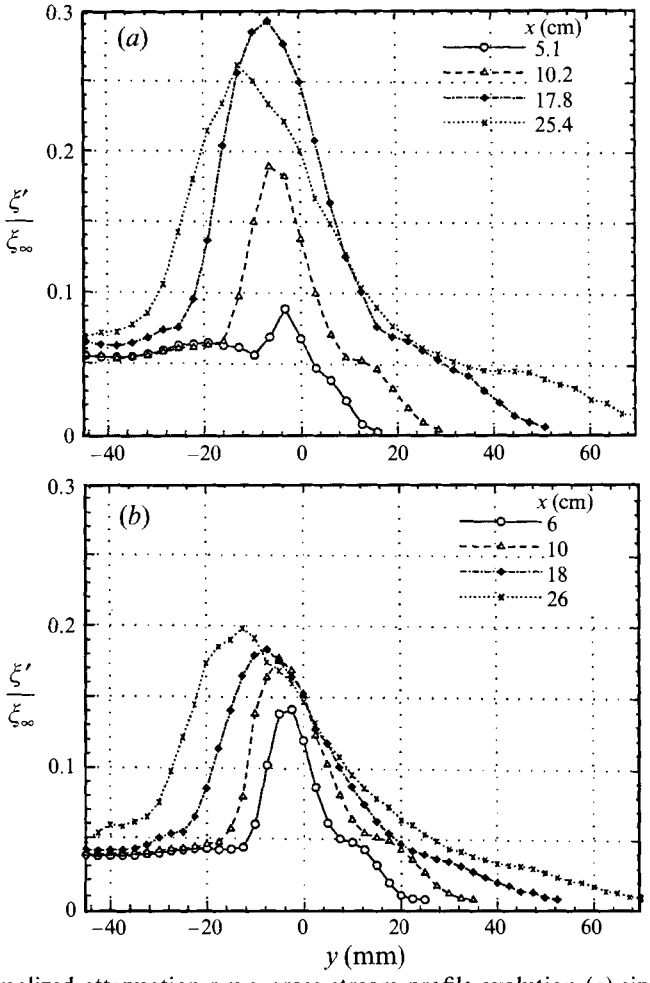

FIGURE 7. Normalized attenuation r.m.s. cross-stream profile evolution (*a*) single frequency forcing (Lázaro & Lasheras 1992*b*), (*b*) pairing mode forcing.

and differences between the two cases. Not surprisingly, the initial profiles have the same peak and plateau-shaped region (figure 7*b*). Further downstream, the peak continues to grow monotonically with no sudden shifts in location (figure 8*c*,*d*), while the prominent plateau is erased during the pairing event. The above results indicate that the streak development is altered by the pairing, and that the streak reconnection observed in the single frequency forcing case never occurs once the pairing is initiated. Thus, it is already becoming evident that the final subharmonic structure produced by the pairing is not similar to the one produced by dispersion due to a single length scale. The history of the flow through the transitional process has significantly altered the final distribution structure. This gives additional support to the somewhat subjective characterizations shown in the attenuation images.

The last set of measurements to be presented as a direct comparison with the single frequency forcing results are those of the time-averaged SMD (figure 9). For the single frequency forcing case, the initial profile decays sharply through the lower edge and then increases slightly at the external edge of the shear layer. Further downstream, the 'valley' region increases, all the while maintaining a location close

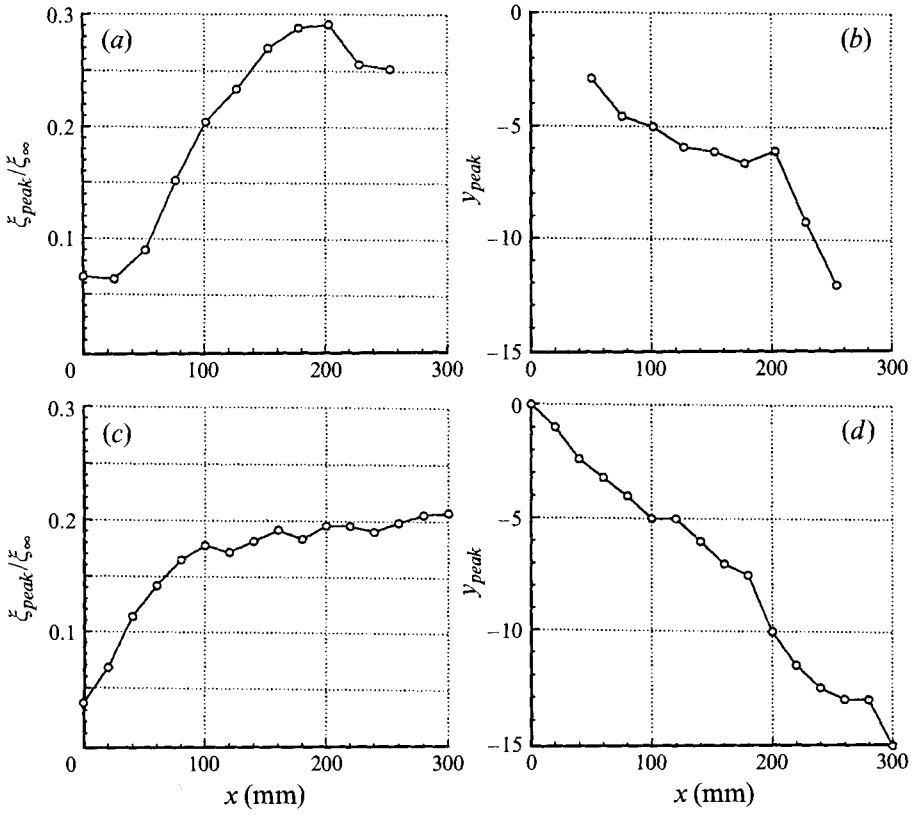

FIGURE 8. Normalized attenuation r.m.s. peak development for single frequency forcing: (*a*) peak amplitude, (*b*) peak cross-stream location (Lázaro & Lasheras 1992*b*) and for pairing mode forcing, (*c*) peak amplitude, and (*d*) peak cross-stream location.

to the centre of the shear layer. This valley is a result of averaging over the depleted core region, which contains only the smallest size droplets. The external recovery can then be attributed to the presence of larger particles in the streak region. As the flow evolves, larger particles continue to respond and migrate through the base of the streak, increasing the minimum size of the 'valley'. In the lower sublayer of the spray, a small overshoot is evident during the late stages of development. This is due to the very large droplets' inability to follow through the stagnation point flow and results in an accumulation of the larger sizes.

Comparing our data to these results, the main differences in the SMD resulting from the pairing are the following.

(i) The location of the minimum starts in a similar location as the single frequency forcing case, but after the pairing moves to a location on the outside region of the shear layer.

(ii) The minimum size in the 'valley' is initially 10–20% greater than the single frequency case, but eventually relaxes to similar sizes.

(iii) The overshoot in the lower sublayer is much more pronounced.

Point (i) provides additional evidence for the argument that larger particles entrained by the smaller streak before pairing are subsequently deposited into the core of the paired vortex structure. With a greater number of large droplets in this area, the average Sauter mean diameter minimum will then be shifted towards the external

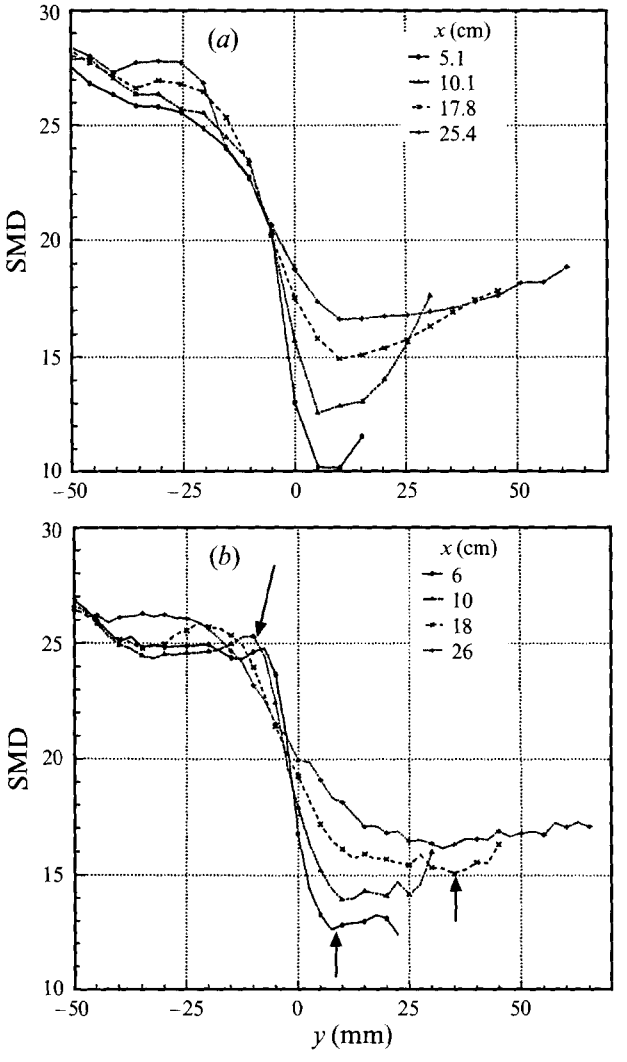

FIGURE 9. Sauter mean diameter (SMD) profile evolution: (*a*) single frequency forcing (unpublished, from same data as Lázaro & Lasheras 1992*b*); (*b*) pairing mode forcing. Note formation of size overshoot in lower sublayer of profile ($y = -0.5$ cm, $x = 6$ cm) and shift in minimum within central region after pairing. Both sets of data were measured with a Malvern laser diffraction sizing instrument.

region. The last two points are most likely due to differences in the initial forcing conditions and slight changes in the initial particle concentration boundary layer thickness.

3.2. *Particulate evolution: dispersive size effects*

In the preceding subsection, the quantification of how the different sized droplets were dispersed during the pairing was limited to the evolution of the time-averaged SMD profiles. While these results were valuable as a direct comparison with previous experimental data, they do not give detailed information about how the various droplet sizes are interacting with the large-scales throughout the pairing event. This information, however, can be observed in the phase-averaged normalized number

Size range (μm)	Size class	Stokes number
$2 < D_0 < 10$	scalar	$St \sim 0.016$
$10 < D_1 < 20$	small	$St \sim 0.098$
$20 < D_2 < 40$	intermediate	$St \sim 0.39$
$40 < D_3 < 100$	large	$St \sim 1.56$

TABLE 1. Size discretization.

frequency, $\eta(D_i, \phi_j; \boldsymbol{x})$. The normalized number frequency is defined from the statistics gathered by the PDPA through the construction of a joint probability distribution function between the phase angle and the droplet size:

$$g(D_i, \phi_j; \boldsymbol{x}) = \frac{n_{ij}(\boldsymbol{x})}{\sum_{i=1}^{S}\sum_{j=1}^{P} n_{ij}(\boldsymbol{x})} \quad \begin{cases} i = 1 \text{ to } S \text{ (number of size classes)} \\ j = 1 \text{ to } P \text{ (number of phase bins),} \end{cases} \tag{3.4}$$

where $n_{ij}(\boldsymbol{x})$ is the number of particles occurring within the size range $D_i \pm \mathrm{d}D/2$ and within the phase angle $\phi_j \pm \Delta\phi/2$ at the location $\boldsymbol{x}$. Looking at a fixed x, we define the normalized number frequency to be:

$$\eta(D_i, \phi_j, y) = \frac{g\,(D_i, \phi_j; y)}{\frac{1}{P}\sum_{j=1}^{P} g\,(D_i, \phi_j; y = -4 \text{ cm})}. \tag{3.5}$$

By normalizing in this manner, deviations in η from unity then indicate changes with respect to the undisturbed free stream in the probability of finding a particle of size D_i over the y and ϕ domain in any given sample.

In the present work, $M = 15$ and $S = 4$ with the size ranges divided as listed in table 1. Here the Stokes number, St (which is the ratio of the droplet's viscous relaxation time to that of the flow fluctuation time scale, $St = \rho_l D^2/(18\rho_g \nu \tau_a)$), of each size class was based upon the fundamental frequency and the average size of the droplets within the given size range. The choice of size range for each class was a compromise to keep the sampling bins large enough to contain a reasonable number of droplets and at the same time to be able to discern differences in their development due to size effects. Even so, our initial droplet size distribution was heavily weighted towards the scalar and small size classes (which accounted for approximately 80% by number of all the particles), while the large size class constituted roughly 4% of the spray in the undisturbed free stream. Considering that each sample contained 10000 points, this does present a sizable amount of statistical uncertainty in the largest size range (approximately 20%). It will be observed, though, that even with this limitation, clear trends for this size are obtained.

3.2.1. *Size dispersion evolution in the presence of a single length scale. Region I*

Examining contours of η at the end of region I (figure 10) shows results that are characteristic of single frequency dispersion. As each one of the surfaces shows, the large-scale streak forms a peaked high-probability ridge, which moves further away from the vortex core and closer to the spray free stream as the size is increased. For the largest size, this peak occurs within the free stream and shows

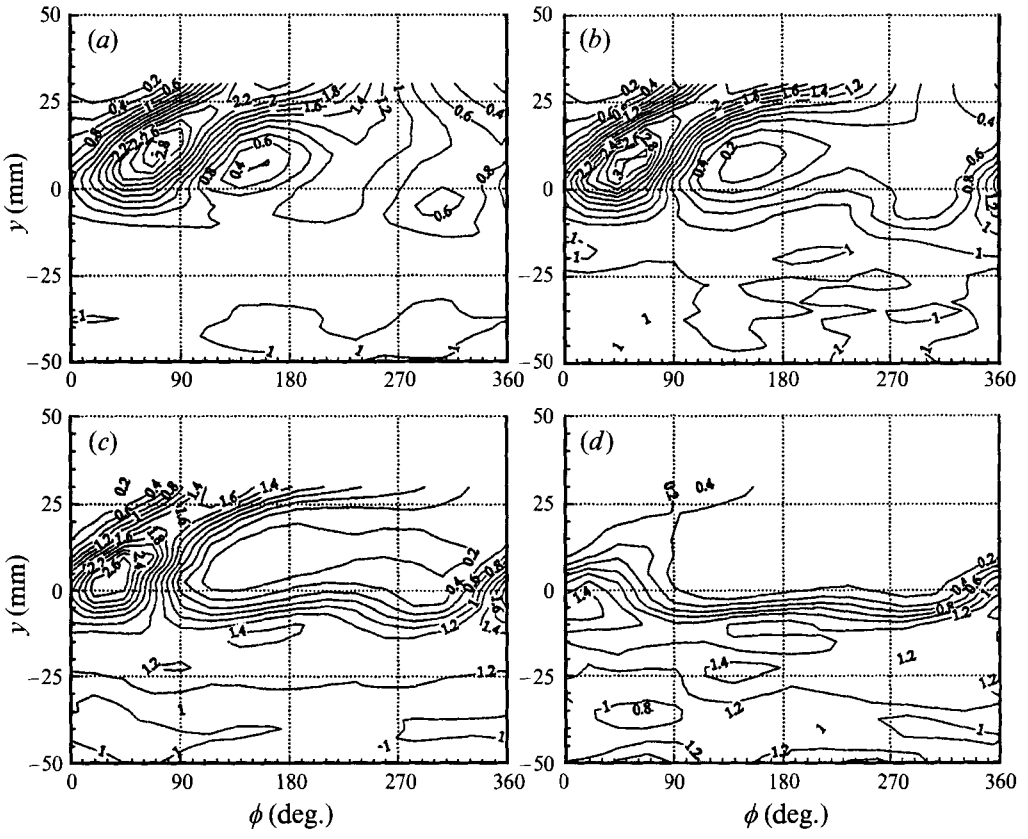

FIGURE 10. Contours of the normalized number frequency at $x = 10$ cm, region I: (*a*) scalar size class, D_0; (*b*) small size class, D_1; (*c*) intermediate size class, D_2; (*d*) large size class, D_3.

very little significant development along the streak. This feature results in a size decay along the streak centreline and a size increase with radial displacement from the vortex core, and is consistent with previous experimental (Lázaro & Lasheras 1992*a*; Longmire & Eaton 1992) and numerical findings (Martin & Meiburg 1994; Chein & Chung 1988). From the previous work, it is known that this size-dependent dispersion can be parameterized by the Stokes number and is a result of increasing inertial effects in the presence of a combined vortex and stagnation point flow. For small Stokes number ($St \ll 1$) the particles follow the flow closely and are entrained along the full length of the streak and into the vortex core. As the droplet size, and hence Stokes number, is increased, the droplets are no longer able to follow the flow and require a longer time to adjust to the disturbance. Hence, the extent of their azimuthal entrainment is retarded compared to droplets of smaller Stokes number and they tend to move along the outer edge of the vortex due to centrifugal effects. Additionally, as a particle with a slow response time is entrained towards a stagnation point, its trajectory will deviate from the fluid streamlines and overshoot into the opposing stream (Martin & Meiburg 1994). This causes the droplet to oscillate between the two streams, slowing its entrainment away from the stagnation point, and results in the accumulation of larger sizes, as observed above (figure 10*d*).

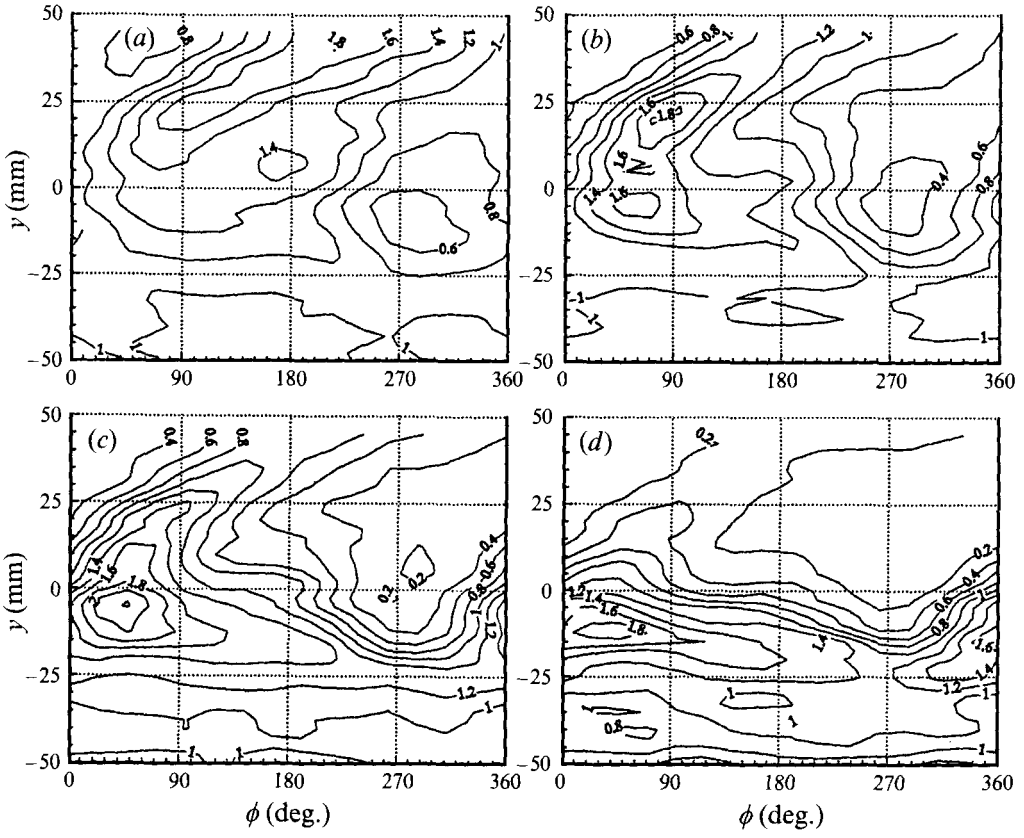

FIGURE 11. Contours of the normalized number frequency at $x = 18$ cm, region II: (*a*) scalar size class, D_0; (*b*) small size class, D_1; (*c*) intermediate size class, D_2; (*d*) large size class, D_3.

3.2.2. *Size dispersion effects of vortex pairing. Regions II and III*

The details of the dispersion during the pairing event can be determined by examining η at a location in the transitional region, $x = 18$ cm (figure 11). As the pairing starts, one can observe that the smaller vortex is pushed downward and the scalar sized particles are drawn down into the high-speed layer. This is substantiated by the formation of a decreased probability hole on the lower right side of figure 11(*a*). The larger particles cannot respond to the pairing this quickly and are disturbed only a small amount (figure 11*b*). For the largest size particles, the pairing process is reduced to the lumping of the two undeveloped streaks in a manner somewhat similar to that observed by Longmire & Eaton (1992).

The resulting subharmonic size distribution is also observed to be dissimilar to structures created by a single dominant frequency. Examining the number frequency of each size class (figure 12) shows what a diverse impact the pairing has produced. The scalar size has experienced a very pronounced homogenization – peak probability values now fluctuate about 30% at any fixed cross-stream location as compared with 150% during the single frequency region. This is to be expected for particles with $St \ll 1$, as their quick response time will allow them to take advantage of the strong mixing that occurs during the pairing process. As the size increases, the resulting homogenization decreases. For the intermediate and large sizes, we once again see the streak and depletion regions that are characteristic of heavy-particles coherent-

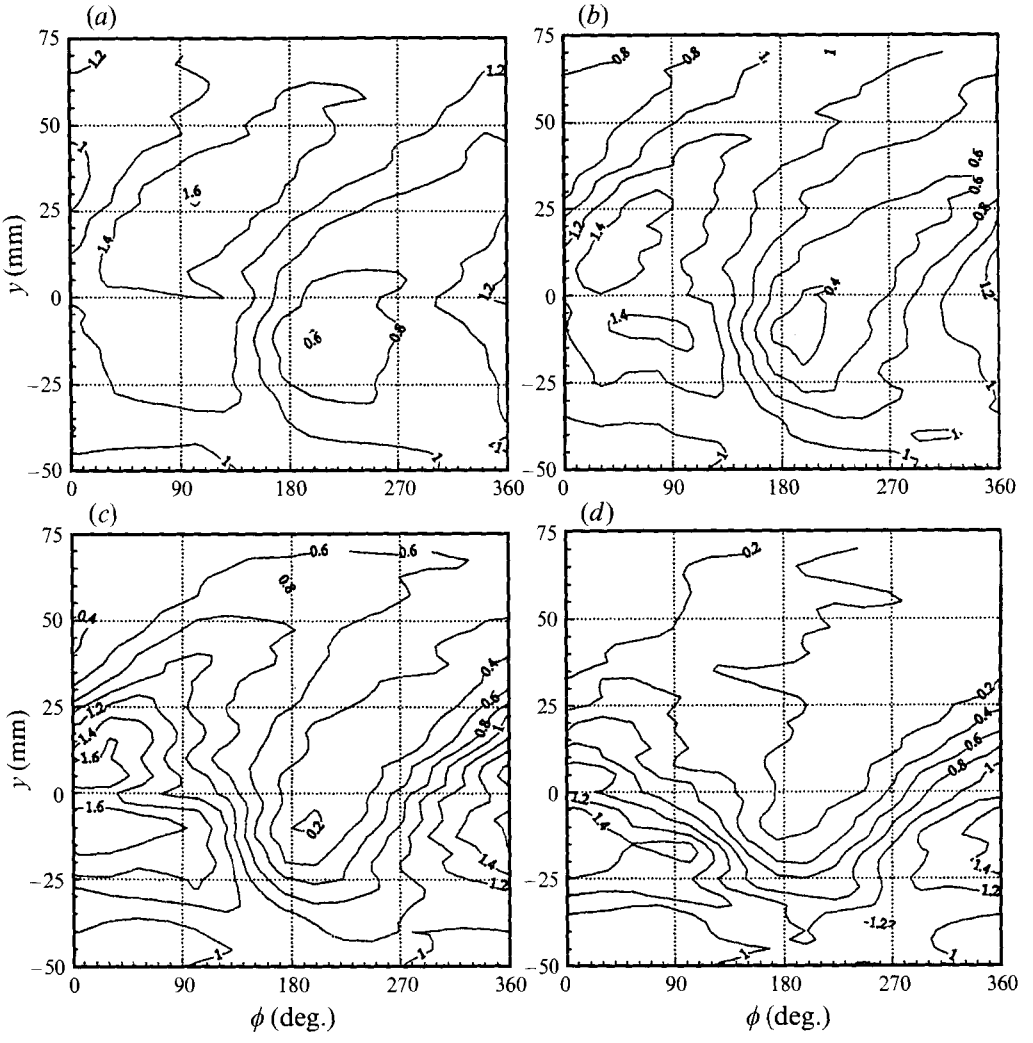

FIGURE 12. Contours of the normalized number frequency at $x = 30$ cm, region III: (*a*) scalar size class, D_0; (*b*) small size class, D_1; (*c*) intermediate size class, D_2; (*d*) large size class, D_3.

structure dispersion (albeit with a shape slightly different as remarked above). Thus, it is noted that the homogenizing influence of the pairing is strongly linked to the response time of the droplets and the driving frequencies of the flow, resulting in complex separation effects.

It should be noted at this point that the above dispersion measurements are the result of the specific pairing event produced by our particular combination of phase and amplitude of the forcing signals. Even so, the trends observed are fairly general and would be qualitatively similar under different forcing conditions. The quantitative differences would then stem from parameters controlling the dispersion that are associated with the details of the pairing event. In addition to the Stokes numbers based on the dominant frequencies (St_1, and St_2), the other two parameters that impact on the dispersion of the individual size classes are: the fundamental development time, τ_1, and the subharmonic lifetime, τ_2 (figure 13).

As was discussed earlier, and shown in the results of Lázaro & Lasheras (1992*b*),

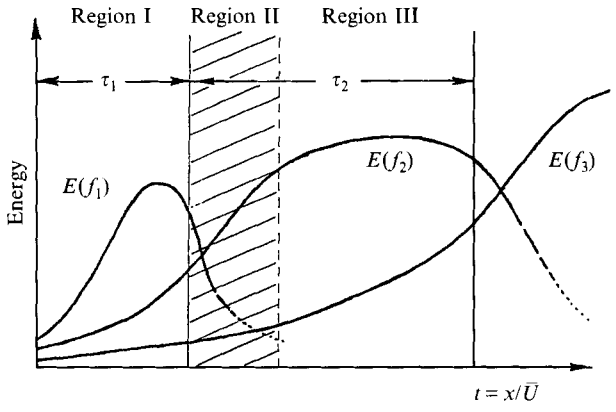

FIGURE 13. Schematic description of time scales determining the extent of particle dispersion in the free shear layer. The lines show the development of the kinetic energy of the fundamental (f_1), first subharmonic (f_2), and second subharmonic (f_3) frequencies of the large-scale structures. Note correspondence to figure 7, showing extended downstream development.

larger Stokes number particles require additional time to adequately respond to fluctuations. This size-dependent time lag was responsible for the azimuthal streak variation in the region dominated by the fundamental disturbance. If the fundamental growth had been allowed more time prior to pairing (larger τ_1), then there would have been more extensive streak development and larger particle dispersion in the intermediate sizes ($St \sim 0.4$). This would have resulted in more extensive homogenization for this size during the pairing, as the inner streak is dispersed throughout the core of the paired vortex. Also, with an increased fundamental development time, there would have been more homogenization in the scalar class even before the pairing event, although to what relative extent cannot readily be determined.

The second parameter of importance, namely the subharmonic lifetime, would determine how long the particles can interact with the paired structure before the next pairing event takes place. This is of significance for the larger particles ($St \sim 1$) ingested during the pairing; namely, if given a sufficient amount of time they would once again be centrifuged towards the periphery of the vortex structure. This radial redistribution process, however, was not observed in our case owing to the lack of significant large-particle development prior to pairing.

In surveying the available literature, it has been noted that particles with a Stokes number of the order unity tend to be dispersed by the coherent structures further than corresponding fluid elements. As discussed above, this did not occur in our particular flow (cf. figures 10*d*, 11*d*, and 12*d*). This is in contrast to numerical results obtained by Chein & Chung (1987), who found that the pairing event increases particle dispersion in comparison to the pre- and post-pairing flows. Our findings, however, do not contradict these results, but instead reflect the fact that their simulations considered groups of particles that were released in small regions in space and time, while our flow continually disperses droplets from all regions in the high-speed stream. Thus, even though certain regions of the structure may be very effective at dispersing particles, the net effect of the whole structure does not result in amplified dispersion properties. This is confirmed by the numerical simulations of Martin & Meiburg (1994), who showed that dispersion integrated over the subharmonic wavelength during the pairing event exhibits a reduced value in comparison to single frequency forced flows. Their results also indicate that no particles are dispersed

further than fluid elements prior to or during the pairing. Only well after the pairing is amplified dispersion observed.

3.3. *Kinetic energy transfer between the two phases*

In the analysis of two-phase, turbulent flows, one of the most pressing obstacles is to effectively model the transfer of linear momentum and kinetic energy between the two phases. Often in numerical computation of these flows, the transfer models rely on algebraic, first-moment closures (Elghobashi & Abou-Arab 1983). In many cases, one must use educated guesses for the resulting coefficients or attempt to model them by fitting the parameters to the limited experimental data currently available. In order to gain an understanding of the underlying physical processes and to assess the validity of any such closure models, it is important to obtain experimental information on the instantaneous fluctuations of all the flow variables. This would enable one to have direct information on how the cross-moments vary throughout the flow, and judge the performance of the models. Current experimental methods, however, do not allow such detailed, complete measurements. In turbulent shear flows, however, where large-scale structures are receptive to controlled perturbation, conditional sampling offers a very effective tool to produce ensemble-averaged portraits of how the closure terms are affected by the large-scale structures. It is for these reasons that we present measurements of the ensemble-averaged kinetic energy transferred between the phases in a turbulent free shear layer.

Following physical reasoning (Williams 1988), the instantaneous kinetic energy transfer per unit volume per unit time to the dispersed phase (spray) from the carrier gas can be written as

$$P(\boldsymbol{x},t) = \int_0^\infty 3\pi\mu D\,(\boldsymbol{u}(\boldsymbol{x},t) - \boldsymbol{v}(D,\boldsymbol{x},t)) \cdot \boldsymbol{v}(D,\boldsymbol{x},t) f(D,\boldsymbol{x},t)\mathrm{d}D, \tag{3.6}$$

where μ is the dynamic viscosity of the gas, $\boldsymbol{u}(\boldsymbol{x},t)$ is the gas velocity, $\boldsymbol{v}(D,\boldsymbol{x},t)$ is the velocity of a droplet of size class D, and $f(D,\boldsymbol{x},t)$ is the number size probability density function (non-normalized) of the spray. The above expression assumes that the dominant force acting on the droplet is due to viscous drag, and that the added mass, Basset force, lift force, etc. are small in comparison. It should be noted that expression (3.6) is not equal to the total sink (or source) of kinetic energy on the continuous phase, as it does not reflect the added viscous dissipation due to the drag force acting on the drops. In addition, there are also other terms which account for the redistribution of potential to kinetic energy due to accelerations of the continuous flow ($D\boldsymbol{u}/Dt + \boldsymbol{g}$), which for most cases of high-inertia particles can be neglected. In our mixing layer, the Reynolds number based on the relative velocity of the droplets is less than 1 for the majority of the spray, but for the largest droplets it is typically around 4, and can be as high as 20. Although using the Stokes drag solution will incur a slight underestimate of the drag for the extreme size and velocity cases, it is a good approximation for most of the spray.

Information regarding the large-scale contribution to the kinetic energy transfer can then be obtained by taking a conditional- or phase-average of (3.6), resulting in

$$\langle P(\phi)\rangle = \int_0^\infty 3\pi\mu D\,\langle(\boldsymbol{u} - \boldsymbol{v}) \cdot \boldsymbol{v} f\rangle\,\mathrm{d}D. \tag{3.7}$$

For a detailed analysis of the kinetic energy equation, and an evaluation of all the interaction terms which appear in its phase-averaged form, the reader is referred to Kiger (1995). The experimental characterization of this quantity poses great

difficulties since there is no instrument available that can instantaneously measure the gas velocity, the particulate velocity, and the size distribution. However, these quantities can be averaged individually, which will allow us to make a good estimate through the approximation

$$\langle (\boldsymbol{u}-\boldsymbol{v})\cdot\boldsymbol{v}f\rangle \sim \big(\langle \boldsymbol{u}\rangle - \langle \boldsymbol{v}\rangle\big)\cdot\langle \boldsymbol{v}\rangle\langle f\rangle . \tag{3.8}$$

As mentioned in §3.1, owing to the periodic nature of the large scales this is quite a good approximation for our flow.

Corresponding to the size groups in table 1, the velocity was then conditionally averaged according to size to obtain $\langle \boldsymbol{v}(D_i,\boldsymbol{x},\phi)\rangle$, $i = 0,1,2,3$. Since we are interested mainly in the large-scale fluctuations, it can be shown† that the velocity of the scalar sized droplets can be used to faithfully represent the velocity of the carrier gas. It then remains to calculate $\langle f(D_i,\boldsymbol{x},\phi)\rangle\,\mathrm{d}D$, the conditionally-averaged concentrations of the different size classes. This is done using laser attenuation data in conjunction with the coarse number distributions obtained from the PDPA. Converting the PDPA number p.d.f.'s to volume p.d.f.'s and using (2.2), the volume fraction of particles within the size range of $D \pm \mathrm{d}D/2$ is given by

$$\alpha(D) = \alpha\,\mathrm{pdf}(D)\mathrm{d}D = \frac{\xi\,\mathrm{pdf}\,(D)\,\mathrm{d}D}{3L\displaystyle\int_0^\infty \frac{\mathrm{pdf}\,(D)}{D}\mathrm{d}D}. \tag{3.9}$$

Similarly, the number concentration of this size class is the volume fraction divided by the average volume of a single particle within that size class:

$$f(D)\mathrm{d}D = \frac{\alpha(D)}{\frac{1}{6}\pi D^3} = \frac{2\xi\,\mathrm{pdf}\,(D)\,\mathrm{d}D}{\pi L D^3\displaystyle\int_0^\infty \frac{\mathrm{pdf}\,(D)}{D}\mathrm{d}D}. \tag{3.10}$$

Thus, the experimental realization of the kinetic energy transferred to size D_i per unit volume per unit time is given by

$$\langle P(D_i,\phi)\rangle = \frac{6\mu\,\langle\xi\rangle\,\langle \mathrm{pdf}(D_i)\Delta D_i\rangle}{\pi L\,\langle D_{30_i}^3\rangle^{2/3}\displaystyle\sum_{j=0}^{3}\frac{\langle \mathrm{pdf}\rangle\,\Delta D_j}{\langle D_{30_j}^3\rangle^{1/3}}}\big(\langle \boldsymbol{u}\rangle - \langle \boldsymbol{v}\rangle\big)\cdot\langle \boldsymbol{v}\rangle , \tag{3.11}$$

and the total energy can then be calculated as

$$\langle P\,(\boldsymbol{x},\phi)\rangle = \sum_{i=1}^{3}\langle P\,(D_i,\boldsymbol{x},\phi)\rangle , \tag{3.12}$$

where D_{30_i} is the volume-average diameter of the size bin i.

Before proceeding to discuss our measurements, it should first be pointed out that there are several sources of error associated with using (3.11) to measure the conditionally averaged kinetic energy transfer given by (3.7). The first source of error is the statistical uncertainty of the data. The largest size had the fewest samples, ranging from 45 to 5 samples per bin. As a worst case example, the uncertainty in the

† If one uses the complete equations of motion to examine the response of a droplet to periodic fluctuations, as was done in Lázaro & Lasheras (1989), it can be readily determined that the smallest size class, D_0, will respond to the higher-frequency, large-scale fluctuation (140 Hz) with $\|\mathbf{u}_p\|/\|\boldsymbol{u}_g\| \geqslant 0.98$.

Size range (μm)	Size class	Approximate peak value and uncertainty (Wm^{-3}), x =6 cm
$10 < D_1 < 20$	small	10 ± 2
$20 < D_2 < 40$	intermediate	30 ± 3
$40 < D_3 < 100$	large	17 ± 2
$\sum D_i$	Total	55 ± 7

TABLE 2. Kinetic energy transfer uncertainty estimation.

velocity of the largest size was typically 4% in the regions where the energy transfer was sizable†. For the small droplets, this uncertainty was much smaller, having an average value of 1%. To estimate the uncertainty in the energy transfer, the statistical convergence of (3.11) and (3.12) was examined in the lower mixing layer boundary. The approximate peak values and average uncertainty for each of the size classes is shown in table 2. The uncertainty was quantified as the amount of variation observed in the energy transfer as the data converged to their final values.

The last two deviations arise from how the PDPA measures the p.d.f. distributions. The first of these errors is due to the fact that the effective probe detection volume increases with the size of the droplet owing to its increased scattering cross-section. Our Aerometrics PDPA uses an empirical algorithm to correct for this error during post-processing. We did not perform similar corrections as the small benefits gained would be outweighed by the increase in error caused by the added manipulations. The second discrepancy results from the fact that the PDPA measures the size distribution in a swept volume, whereas the attenuation uses the instantaneous volume occupied by the entire beam. If there is a large mean velocity bias between the various sizes, then the p.d.f. will be skewed toward the higher speed particles in proportion to the velocity differences between the sizes. In this experiment, this effect will only be sizable when the mean velocity becomes close to the same order of magnitude as the slip velocity between different sizes, say $|(\boldsymbol{v}(D_i) - \boldsymbol{v}(D_j))| / |\boldsymbol{v}(D_j)| < 0.2$, which will not occur until one reaches the low-speed portion of the mixing layer where the concentration of droplets approaches zero.

Even taking into account the above shortcomings, we are confident that the conditional-averaged data measured in this way show distinctive trends which reveal the underlying physics of the particle dynamics, and which also represent the best currently available data for modelling purposes. In the following section we will discuss the conditional-averaged kinetic energy transfer between the liquid and gas phases as a function of particle size, beginning with the evolution of the dominant fundamental disturbance, leading through the pairing event, and finishing with the later stages of development of the resulting subharmonic structure.

3.3.1. *Fundamental-dominated flow: role of a single vortex*

The kinetic energy transfer between the phases in the initial flow region exhibits the relevant features of the transfer processes that are basic characteristics of the large-scale structures present in the shear layer (figure 14). Perhaps the most surprising fact is that most of the energy exchange does not take place in the central region of the mixing layer as might be expected, but instead occurs in a sublayer just outside the

† The uncertainty peaked around 20% in the external region of the shear layer, but here the concentration of droplets was extremely small, and hence the energy transfer went to zero.

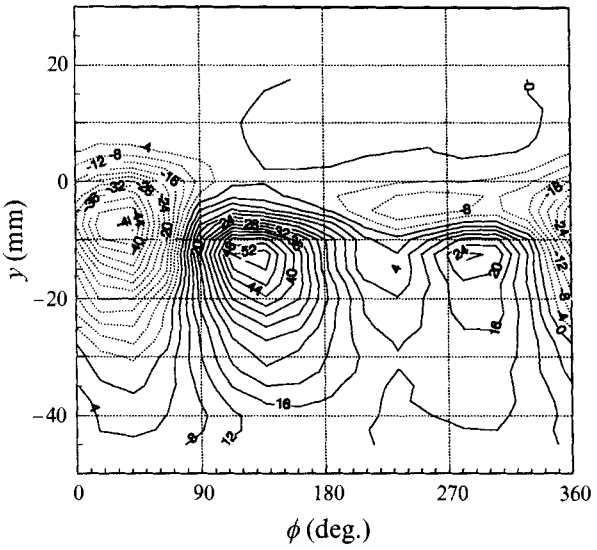

FIGURE 14. Contours of the conditional-averaged total kinetic energy transfer to the dispersed phase at $x = 6$ cm, region I. Note the three concentrated peaks forming in a sublayer beneath the coherent structures: peak 1, ($\phi = 30°$, $y = -0.75$ cm); peak 2, ($\phi = 130°$, $y = -1.25$ cm); peak 3, ($\phi = 290°$, $y = -1.25$ cm). Units are in $\mathrm{W\,m^{-3}}$.

mixing region and extends deep into the free stream of the spray. It is readily apparent that the transfer in this region is characterized by large, structured inhomogeneities with both positive and negative transfer regions which form as the dispersed phase locally absorbs and restores energy to the carrier fluid. Comparing the energy transfer plots with those of the attenuation (figure 6) and the velocity field (figure 3) indicates that the positive peak is located under the core of the vortex structure, while the negative peak occurs beneath the free stagnation point located in the braid region between successive vortices. Upon further comparison with the r.m.s. velocity field in figure 3, it is found that the kinetic energy transfer maxima are also outside the region of the peak velocity fluctuations, which is in contrast to what might be assumed in more traditional turbulence modelling. This then poses an interesting question: if the turbulent Reynolds stresses are not responsible for this energy exchange, then what is the source of the maxima? All of the above experimental evidence indicates that the kinetic energy transfer peaks are the result of two effects.

(i) The droplet concentration field is inhomogeneous across the mixing layer and quite dilute in the external region of the flow.

(ii) There are peaks in the slip velocity field due to the droplets' response to a periodic forcing by distributions of lumped vorticity in the mixing layer.

The presence of the vortices creates an irrotational perturbation velocity in the free stream that decays inversely with distance from the mixing region (figure 15). For the streamwise velocity component, this perturbation will be a maximum beneath the vortex core, with a corresponding minimum beneath the stagnation region between the two vortices. If it is assumed that the coherent structures are moving at approximately the mean speed of the two layers, then the particles outside the shear layer in the uniform stream will be convected past them at a relative frequency of $f' = f(U_2 - U_1)/(U_2 + U_1)$. When a droplet initially moving at a steady velocity is exposed to this alternating velocity field, it will try to follow the disturbance with varying

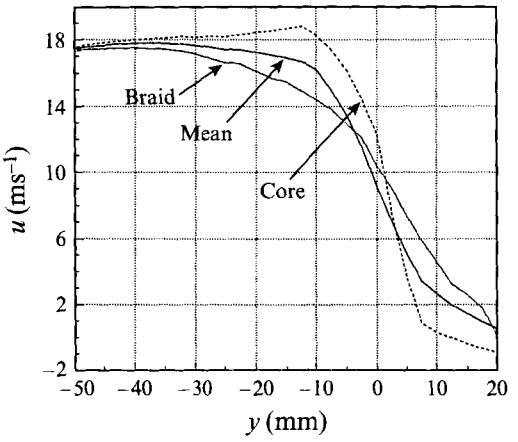

FIGURE 15. Conditional-averaged streamwise velocity profiles at $x = 6$ cm, showing the average velocity increase at the core, $\phi = 121°$, and the deficit at the braids, $\phi = 25°$.

amounts of success depending on its relative Stokes number, $St' = \rho_l D^2 f'/(18\rho_g \nu)$. This sets up slip velocities in the direction of the particle's motion and creates the observed pattern of the kinetic energy transfer. Additional evidence for this will be presented when we consider the effects of the droplet size on the kinetic energy transfer. The fact that this mechanism of kinetic energy transfer exists should come as no surprise; rather, the interesting point is what *prevents* the central mixing region (with the maximum fluctuation levels) from making a sizable contribution? The answer to this lies in the details of the concentration field (approximately given by the attenuation, figure 6) and the dot product of the droplet velocity with the slip velocity (figure 16). There it can be seen that even though the slip velocity is at a maximum in the external mixing region (approximately twice the corresponding value at the observed energy transfer peaks), the absolute value of the droplet velocity and the droplet concentration is so low that it does not produce any significant energy transfer. Additionally, in between the two peaks there is a region where the concentration and slip velocity are large, but the vector product $(\boldsymbol{u} - \boldsymbol{v}) \cdot \boldsymbol{v}$ is small owing to the strong lateral velocity fluctuations of the vortex. Finally, there is a region in the central mixing layer on the lower edge of the vortex core where the velocity vector product does exhibit a peaked minimum, but again the concentration is too small to produce a sizable kinetic energy transfer. This negative vector product peak results from the steep velocity gradients around the core as well as the particle's inertial 'memory' of the high-speed free stream. In the initial developing region, the concentration of particles in the streak near the core is too low for this mechanism to have any impact, but as will be seen, this region makes a slight contribution in the later development.

Since it has been shown in the previous subsections that the particle size plays a dominant role in the dispersion process, it is of paramount interest to also determine how the different size classes contribute to the total kinetic energy transfer. Upon examination of the energy transfer for each of the sizes (figure 17), it is seen that the overall pattern of the peaks and valleys is preserved for each size, with slight differences in the location and relative proportion of each size's contribution. When comparing the magnitudes of the these peaks, it is evident that there is a distinct ordering of the magnitude based on size, with the greatest contribution coming from the intermediate size, followed by the largest size, and then finally the smallest. The

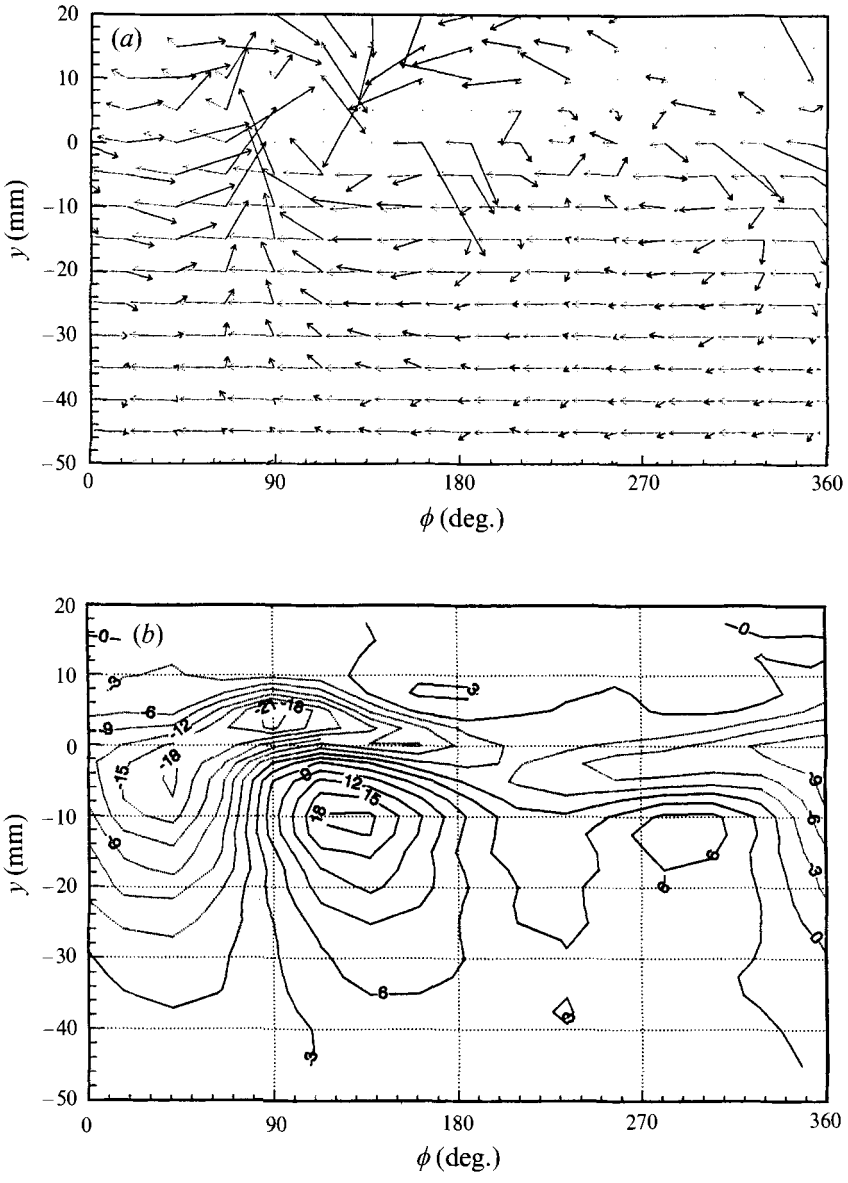

FIGURE 16. Conditional-averaged velocity vectors and dot product of absolute droplet and relative slip velocity of the intermediate size, D_2, at $x = 6$ cm. (*a*) Solid vector: slip velocity, 24° = 1 m s^{-1}; dashed vector: absolute velocity, 24° = 18 m s^{-1}. (*b*) Isocontours of the velocity dot product, $(\boldsymbol{u} - \boldsymbol{v}) \cdot \boldsymbol{v}$. Units are in m^2 s^{-2}.

ordering of the peak magnitude is influenced by the Stokes number through its connection with the magnitude of the slip velocity. The larger the Stokes number, the greater the slip velocity and hence greater energy transfer. The drop-off in concentration of the largest Stokes number droplets then eventually balances the increased slip velocities and results in a specific ordering of the peaks as noted above. In addition to the differences in magnitude, the locations of the peaks all shift downstream (lower phase angles) as the size is increased. This temporal shift of

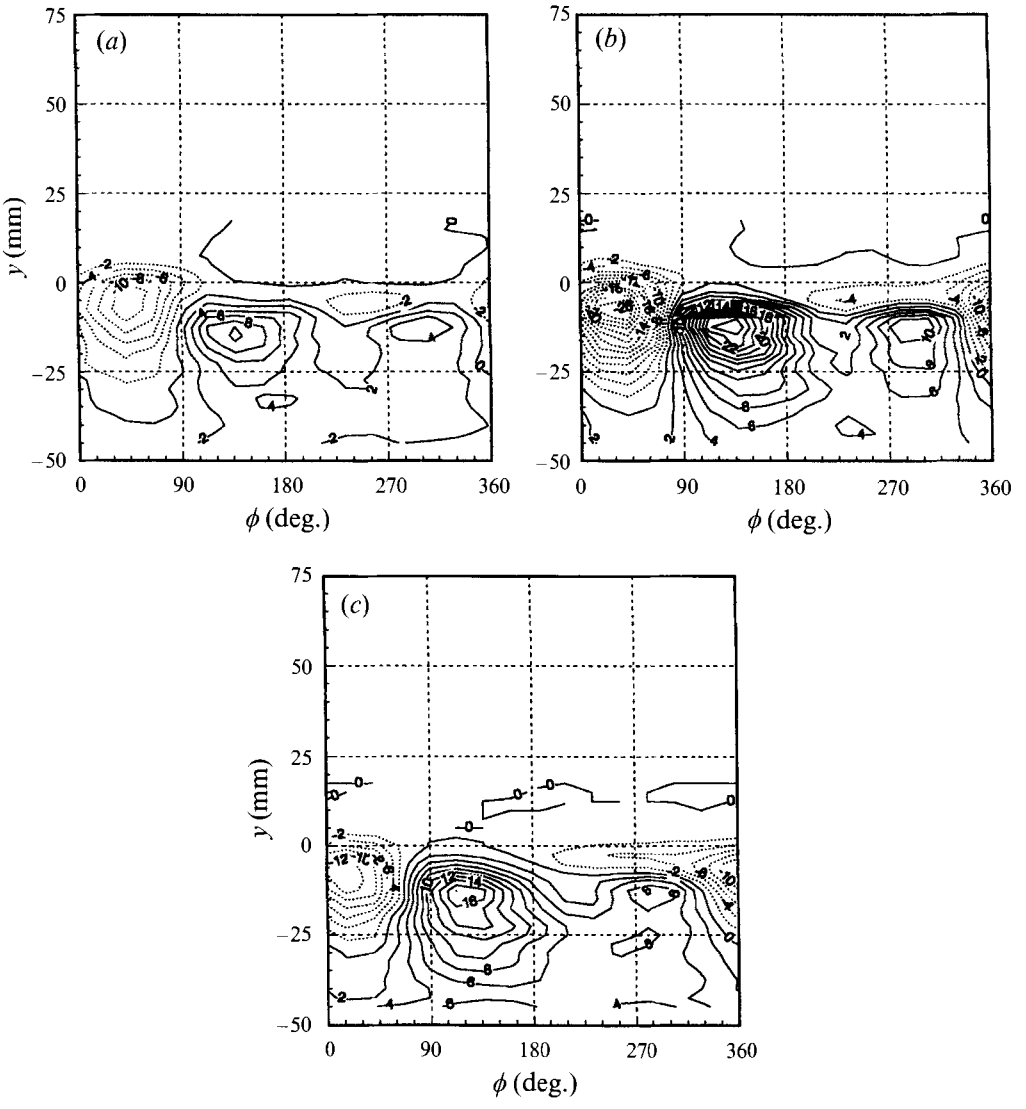

FIGURE 17. Conditional-averaged kinetic energy transfer for the different size classes at $x = 6$ cm, region I: (*a*) small size class, D_1; (*b*) intermediate size class, D_2; (*c*) large size class, D_3. Units are in W m^{-3}

the peak's location can also be consistently explained by Stokes number arguments. For the three size classes considered, the average relative Stokes numbers based on $f_1' = 140$ Hz are approximately 0.1, 0.4, and 1.6 for the small, intermediate, and large classes respectively. Using the equation of motion for an isolated particle, it is possible to obtain analytical expressions that describe the steady-state response of the particle to a periodic disturbance (Hjelmfelt & Mockros 1966). The outcome of such an analysis for the given particles result in phase differences of 28°, 60°, and 70° (14°, 30°, and 35° on the subharmonic scale shown in the figure) between the scalar sized droplets and the larger size classes. Examining the particle response velocity measured in the flow (figure 18) shows that the measured phase lags are approximately 15°, 25°, and 45° (±7° based on bin width) which agrees quite closely

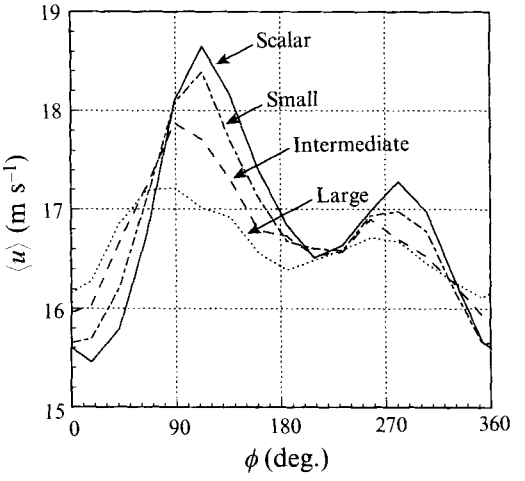

FIGURE 18. Conditional-averaged streamwise velocity component for each size class at $x = 10$ cm, $y = -1.5$ cm, showing the amplitude decrease and phase lag between the sizes.

with the predictions. Discrepancies between the results can be explained by: (i) the uncertainty in the waveform shape, (ii) the largest size droplets will not be able to attain a steady-state response, as the transient time scale is of the same order of magnitude as the evolution time, and (iii) the fact that the flow is not composed of a single frequency – even though the fundamental is dominant, there is some finite contribution from the subharmonic.

3.3.2. *Vortex pairing event and resulting subharmonic structure*

Knowing that the vortex pairing plays a dominant role in different dispersion properties of the droplets depending on their size, it is also of interest to quantify how the energy transfer occurs during this transition. Questions that are raised by knowledge gained in the previous subsections include the following. How does the competition of a second flow scale affect the kinetic energy transfer process? Once the flow is back to a single dominant scale (this time twice as large), will the mechanism still be the same? Finally, can we use this information to infer what might take place further downstream in the mixing layer, after several pairings have occurred?

During the initial stages of the shear layer development, the peaks of the energy transfer identified in the previous section displayed a continual increase in magnitude (figure 19). From the mechanism described previously this can be ascribed to an increase in the circulation within the core of the spanwise rollers as they continually remove vorticity from the braid region (Corcos & Sherman 1984). This vorticity intensification increases the strength of the vortex and hence heightens the fluctuating velocities perceived by the droplets in the free stream. When the pairing begins, the peak levels are observed to decrease and maintain a reduced amplitude throughout the rest of the test section. The reason for this decrease can be explained primarily by the growth of the subharmonic length scale and the resulting decrease in the relative Stokes number, increasing the particles' ability to respond to the fluctuations. In addition to this, the vorticity in the core after the pairing does not immediately attain the same concentrated distribution that it had after the initial roll-up, and hence could also contribute to a loss of velocity fluctuation in the free stream. If one follows the location of the peaks throughout the pairing (figure 20) it can be seen that the peaks track with the location of the dominant vortex core and stagnation points

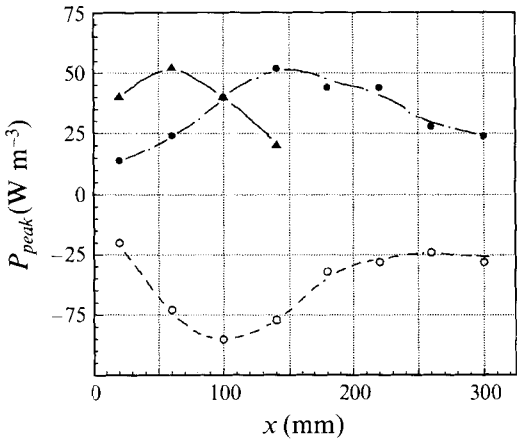

FIGURE 19. Evolution of the amplitude of the three dominant kinetic energy transfer peaks identified over one subharmonic wavelength. ○, peak 1; ▲, peak 2; ●, peak 3 (see figure 14).

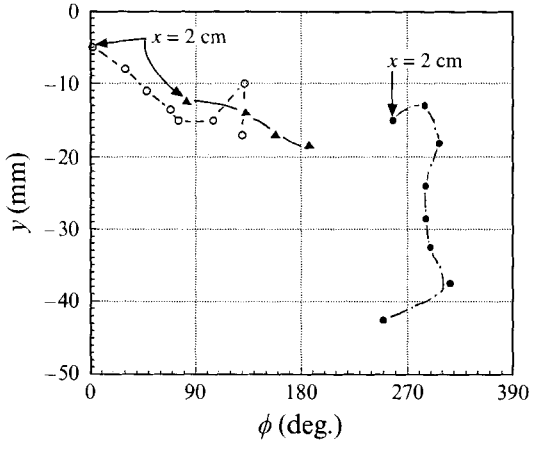

FIGURE 20. Evolution of location of dominant kinetic energy transfer peaks in the (y, ϕ)-plane. Δx between points = 4 cm. ○, peak 1; ▲, peak 2; ●, peak 3 (see figure 14).

of the flow, all the while remaining close to the edge of the sublayer. The positive peak initially formed by the larger fundamental vortex is seen to be obliterated in the early stages of the pairing event, and instead favours the growth of the positive peak located under the smaller vortex. By the end of the pairing, we are left with a positive peak located well into the free stream, and a negative peak that appears to have encroached somewhat deeper into the large-scale streak structure shown earlier.

The pairing event also has an effect on the magnitude of the peaks for each size class and produces a reshuffling of the size responsible for the dominant energy transfer. In our case the flow conditions were such that the large size became the dominant transfer group for the positive peak (figure 21*a*). This is again consistent with a reduction of the relative Stokes number, and the low-pass filtering characteristics of the droplet's amplitude response (see Lázaro & Lasheras 1989). This reshuffling, however, did not appear to occur in the negative peak (figure 21*b*). Instead, all three peak levels seemed to reach somewhat similar values. The equalization of the negative peaks can be consistently explained by the increased concentration of smaller sizes in the core due to the pairing event. As was noted earlier, the velocity vector product

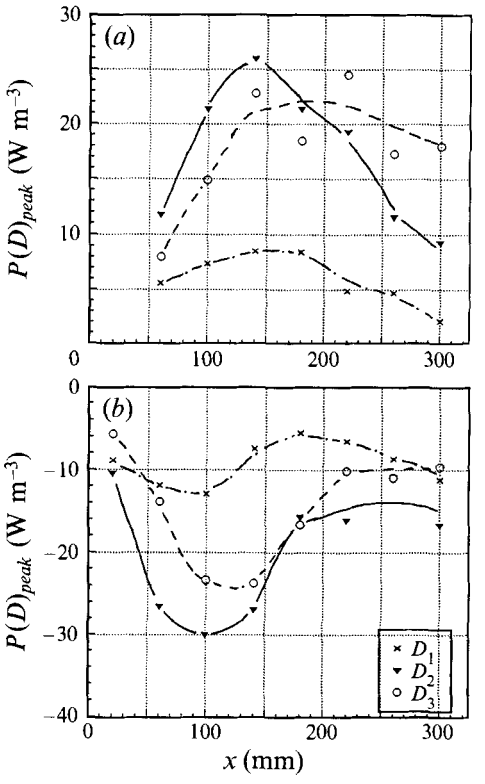

FIGURE 21. Kinetic energy transfer peak amplitude growth for each size class: (*a*) positive peak beneath vortex cores, peak 3; (*b*) negative peak near braid region, peak 1.

exhibited a minimum in this region (strong transfers from the particles to the gas), and hence, the increased concentration of the small droplets shifts the peak kinetic energy transfer towards the vortex core. The large sizes, however, accumulate near the stagnation point and thus reduce the peak energy transfer near the core (figure 22).

What then does this imply for the continued evolution of energy transfer in the mixing layer? The results of the above subsections indicate that the peaked sublayer pattern is a dominant transfer mechanism as long as the vortices maintain a minimum intensity and the relative Stokes numbers of the particles in the spray are at least $O(1)$. Successive pairings increase the structure size and continually decrease the relative Stokes number. As this occurs, the sublayer transfer by the smaller particles decreases to negligible values, leaving contributions mainly due to the larger droplets. Eventually, the large scales grow to a point where all droplet sizes of the spray follow the large-scale fluctuations. When this occurs, a secondary mechanism may be responsible for the kinetic energy transfer between the phases as the Stokes number will most likely be $O(1)$ for some scales present in a turbulent mixing layer. This is further aided by the fact that the homogenization of particles throughout the large-scale structure is greatly enhanced by the decrease in the relative Stokes number, creating increasing concentrations in regions where the particulate interact with the smaller scales. In the case of higher void fractions, this may result in a transfer process which could affect the development of the flow as kinetic energy is redistributed into a region near the braids from beneath the core of the vortex.

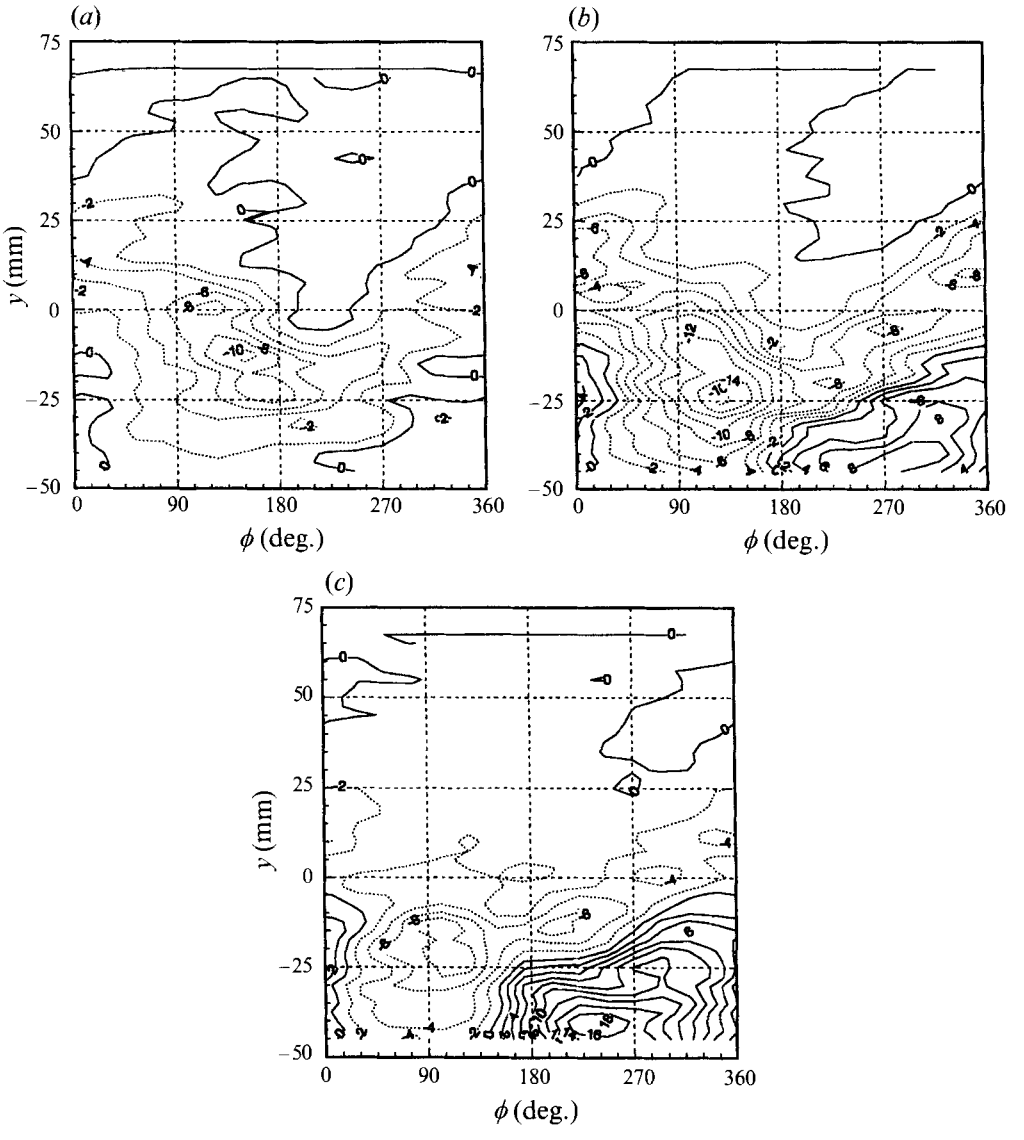

FIGURE 22. Conditional-averaged kinetic energy transfer of the paired subharmonic vortex ($x = 30$ cm, region III) for each size class. Units are in $\mathrm{W\,m^{-3}}$. (*a*) Small size class, D_1; (*b*) intermediate size class, D_2; (*c*) large size class, D_3.

4. Conclusions

The measurements of the velocity and particle concentration fields in a polydispersed, particle-laden, turbulent mixing layer confirm the early observations that the large-scale eddies are primarily responsible for the particle dispersion process. In addition, we found that through the mechanism of vortex pairing the particle concentration field is progressively homogenized as particles entrained by nearby vortices are redistributed inside the resulting subharmonic structure. The homogenization resulting from this process indicated not only a strong dependence on the particle size and dominant eddy time scale, but also on the time between pairing events. Specifically, the fundamental development time, τ_1, controls the growth of each size

class along the initial streak and hence the amount of homogenization attained after the pairing. The time between pairing, τ_2, determines whether or not the subharmonic structure will redistribute larger particles away from the core where they had been deposited by the pairing process.

It was also found that both prior to and during the vortex pairing event, the kinetic energy transfer between the phases due to quasi-steady viscous drag on the particle is a highly anisotropic process. In the early stages of the evolution, where the flow is dominated by a single, large, eddy scale, we found the somewhat surprising result that most of the kinetic energy exchanged between the phases occurs in a region outside the mixing layer and does not coincide with the regions of the maximum velocity fluctuations of the carrier gas. Instead, the transfer is manifested as clearly defined positive and negative peaks existing beneath cores and free stagnation points of the vortices. This mechanism is the result of the particulate's response to the irrotational velocity perturbation fields set up in the free stream by the array of large-scale vortices. Furthermore, it is found that the central region is excluded as a prominent transfer area owing to its lower concentrations as well as regions of strong lateral slip velocity which are not aligned with the droplet's velocity.

The contribution of each size class to the kinetic energy transfer is also linked to the size as well as the concentration of each size family. The maximum contribution is produced by the balance between increasing slip velocity due to particle inertia and the eventual decrease in concentration dictated by the spray's size distribution. The pairing event results in a decrease of the energy transfer, as the growth of the subharmonic introduces a reduced relative Stokes number that is half the size of the initial one. The doubling of the dominant scale also changes the size class which is responsible for the dominant energy transfer as a new slip velocity and concentration balance are formed.

Finally, it is speculated that the above mechanism will remain a significant source of kinetic energy transfer as long as the large scales are maintained and the relative Stokes numbers based on these scales are of order unity. As the pairing continues to reduce the large-scale slip velocities and the homogenization of the particles is increased, additional sources of transfer will likely take place in the braid region where the concentration is increasing owing to the origin of the dispersion streaks. It should also be noted that the kinetic energy measurements presented here only reflect contributions due to a quasi-steady Stokes drag force. In regions where the flow scales approach the same order as the size of the particles, there may be other important factors influencing the kinetic energy transfer between the phases.

The authors wish to thank Dr Benigno J. Lázaro and Dr Paul M. Rightley for their insightful comments and discussion throughout the work. This project was supported by a gift from the United Technologies Corporation and the National Defense Science and Engineering Graduate Fellowship Program.

REFERENCES

BACHALO, W. D. & HOUSER, M. J. 1983 Phase/Doppler spray analyzer for simultaneous measurements of drop size and velocity distributions. *Opt. Engng* **23**, 583–590.

BROWN, G. L. & ROSHKO, A. 1974 On density effects and large structure in turbulent mixing layers. *J. Fluid Mech.* **64**, 775–816.

CHEIN, R. C. & CHUNG, J. N. 1987 Effects of vortex pairing on particle dispersion in turbulent shear flows. *Intl J. Multiphase Flow* **13**, 785–802.

CHEIN, R. C. & CHUNG, J. N. 1988 Simulation of particle dispersion in a two-dimensional mixing layer. *AIChE J.* **34**, 946–954.

CORCOS, G. M. & SHERMAN, F. S. 1984 The mixing layer: deterministic models of a turbulent flow. Part 1. Introduction and the two-dimensional flow. *J. Fluid Mech.* **139**, 29–65.

CROWE, C. T., CHUNG, J. N. & TROUTT, T. R. 1988 Particle mixing in free shear flows. *Prog. Energy Combust. Sci.* **14**, 171–194.

DRAIN, L. E. 1980 *The Laser Doppler Technique.* Wiley.

ELGHOBASHI, S. E. & ABOU-ARAB, T. W. 1983 A two-equation turbulence model for two-phase flows. *Phys. Fluids* **26**, 931–938.

HJELMFELT, A. T. & MOCKROS, L. F. 1966 Motion of discrete particles in a turbulent fluid. *Appl. Sci. Res.* **16**, 149–161.

HUANG, L. S. & HO, C. M. 1982 Subharmonics and vortex merging in mixing layers. *J. Fluid Mech.* **119**, 443–473.

HUSSAIN, A. K. M. F. & ZEDAN, M. F. 1978 Effects of the initial condition on the axisymmetric free shear layer: Effects of the initial momentum thickness. *Phys. Fluids* **21**, 1100–1112.

KIGER, K. T. 1995 Particle dispersion and inter-phase kinetic energy transfer in a turbulent, two-phase shear layer. PhD dissertation, University of California, San Diego.

LASHERAS, J. C. & TIO, K. K. 1994 Dynamics of a small spherical particle in steady two-dimensional vortex flows. *Appl. Mech. Rev.* **47**, 6, part 2, 61–69.

LÁZARO, B. J. 1989 Particle dispersion in turbulent free shear flows. PhD dissertation, University of Southern California.

LÁZARO, B. J. & LASHERAS, J. C. 1989 Particle dispersion in a turbulent, plane, free shear layer. *Phys. Fluids* A **1**, 1035–1044.

LÁZARO, B. J. & LASHERAS, J. C. 1992*a* Particle dispersion in a developing free shear layer. Part 1. Unforced flow. *J. Fluid Mech.* **235**, 143–178.

LÁZARO, B. J. & LASHERAS, J. C. 1992*b* Particle dispersion in a developing free shear layer. Part 2. Forced flow. *J. Fluid Mech.* **235**, 179–221.

LONGMIRE, E. K. & EATON, J. K. 1992 Structure of a particle-laden round jet. *J. Fluid Mech.* **236**, 217–257.

MARTIN, J. E. & MEIBURG, E. 1994 The accumulation and dispersion of heavy particles in forced two-dimensional mixing layers. 1. The fundamental and subharmonic cases. *Phys. Fluids* A **6**, 1116–1132.

MCLAUGHLIN, D. K. & TIEDERMAN, W. G. 1973 Biasing correction for individual realization of laser anemometer measurements in turbulent flows. *Phys. Fluids* **16**, 2082–2088.

SANKAR, S. V. & BACHALO, W. D. 1991 Response characteristics of the phase Doppler particle analyzer for sizing spherical particles larger than the light wavelength. *Opt. Engng* **30**, 1487–1496.

WILLIAMS, F. A. 1988 *Combustion Theory*, 2nd edn. Addison-Wesley.

WINANT, C. D. & BROWAND, F. K. 1973 Vortex pairing: the mechanism of turbulent mixing layer growth at moderate Reynolds number. *J. Fluid Mech.* **63**, 237–255.

YANG, Z. & KARLSSON, S. K. F. 1991 Evolution of coherent structures in a plane shear layer. *Phys. Fluids* A **3**, 2207–2219.